ACS APPLIED MATERIALS & INTERFACES

Research Article

www.acsami.org

Energetic-Assisted Scanning Thermal Lithography for Patterning Silver Nanoparticles in Polymer Films

Chun-Min Huang, Chung-Hsien Yeh, Lung Chen, De-An Huang, and Changshu Kuo*

Department of Materials Science and Engineering, National Cheng Kung University, Tainan 701-01, Taiwan

Supporting Information

ABSTRACT: Energetic-assisted scanning thermal lithography (SThL) was demonstrated with the addition of benzoyl peroxide (BPO) for patterning silver nanoparticles. SThL samples were prepared by spin-coating poly(methyl methacrylate) (PMMA) thin films preloaded with BPO and silver nitrate precursors. Localized thermal analysis via probe heating demonstrated that the BPO decomposition in the polymer film took place at the temperature of 80 °C. Above this temperature, the thermal probe initiated the decomposition of the peroxide, which resulted in the in situ discharge of exothermal energy to compensate the joule shortage and the rapid cooling in the SThL thin film samples. The additional joule energy thermally enhanced the synthesis of silver nanoparticles, which were patterned and embedded in the PMMA thin film. Surface plasmon resonance scattering of these silver nanoparticles was observed by dark-field optical microscopy, whereas the nanoparticle distribution was examined by transmission electron microscopy. Variations in the scanning probe temperatures and peroxide concentrations were carefully investigated to optimize the thermal lithography efficiency upon the addition of energetics.

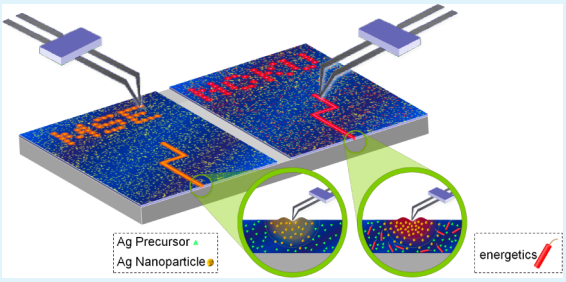

KEYWORDS: *scanning thermal lithography, local thermal analysis, energetics, peroxides, silver, nanoparticles*

INTRODUCTION

Scanning probe lithography (SPL), as an extension of scanning probe microscopy (SPM), facilitates the direct fabrication of high-spatial-resolution features on a material surface without requiring masks or vacuum facilities.[1,2] A precisely positioned scanning probe either constructs a programmed contour drawing or compiles a two-dimensional diagram via sequential "stamping" processes. Versatile patterning mechanisms have been conducted using different SPL probes. For example, a destructive patterning was performed by mechanically scratching a diamond-reinforced SPL probe on a soft polymer surface.[3] In situ surface oxidation was adapted for anodic scanning lithography, wherein an electrically biased probe performs the surface patterning.[4] Near-field optical lithography demonstrated the high-resolution patterning versus the photoinduced cross-linking reaction.[5] Nondestructive SPL has also been achieved using a cantilever equipped with a microfluidic system in so-called dip-pen lithography.[6,7] Molecular deposition and patterning have been accomplished primarily for biorelated applications.

In addition, a localized heating mechanism was introduced to the scanning probe in scanning thermal lithography (SThL). The desired chemical or physical reactions can be triggered by a thermal probe at a given temperature. Temperature-sensitive reactions, such as melting, crystallization, thermal decomposition, or other chemical reactions, can be utilized for SThL fabrication.[8−10] In SThL, joule heat exchange is limited by the low contact area of the thermal probe with the sample surface, which is typically in the range of micrometer to tens of nanometers for the probe tip radius. In the case of polymer-based samples, it was estimated that only approximately 0.1−1.5% of the power generated by the thermal probe is directed to the sample.[11,12] The majority of joule conduction is dissipated to the surroundings, including the substrate, atmosphere, and the probe itself. The net energy that actually initiates the desired SThL reaction is believed to be even lower. Therefore, a successful SThL process is determined by the competition between interfacial cooling and total joule density. This can be mitigated by using a higher heat flux from the thermal probe or the diminished cooling effect. The former generally requires a higher probe temperature or a slower probe lithography rate, whereas the latter involves vacuum SThL[13] or the use of a low thermal conductivity substrate with a lower heat sink effect.[14] For example, a transparent and heat-resistant polyimide film offers a thermal conductivity approximately four times lower than a typical glass substrate.

In this research study, an alternative approach was demonstrated using a novel energetic-assisted SThL process with an extra joule energy source. Distinct from the so-called self-propagating high-temperature synthesis (SHS),[15,16] in which the sustained combustion energy propels the bulk material to very high temperatures, SThL fabrication

Received: October 11, 2012
Accepted: December 5, 2012
Published: December 5, 2012

encounters fast interfacial cooling with poor heat accumulation in a thin film structure. Naturally, the conductive cooling is dependent on the differential temperature (ΔT) and the time (τ). Therefore, the heat accumulation and the localized temperature increase in SThL can be achieved by the addition of an energetic reagent that provides a high energy density, i.e., the compound that generates substantial joule release in a short period of time. Tracking the thermal probe pathway, the in situ energetic decomposition discharges the extra joule energy and raises the localized temperature even higher than the source temperature of the thermal probe itself. Desired chemical reactions can be efficiently initiated at a relatively low probe lithography temperature. Moreover, the confined joule energy and the highly localized heating at the thermal probe tip decrease the possibility of thermally induced damages to the substrate and other neighboring components. The decomposition products of energetic residues or other reaction byproducts can also be easily degassed from the SThL thin film sample.

Energetic peroxides, such as benzoyl peroxide (BPO), are ideal reagents for energetic-assisted SThL. Compared with nitro- or nitrate-based energetics, low molecular weight organic peroxides have moderate energy densities (800−2200 J/g), low decomposition temperatures (70−100 °C), and good compatibilities with organic solvents or polymers. In the following investigations, the SThL samples were prepared by spin-coating poly(methyl methacrylate) (PMMA) thin films preloaded with energetic BPO and silver nitrate ($AgNO_3$). Silver nitrate served as the nanoparticle precursor, which was thermally converted to silver nanoparticles (Ag NPs). The resulting particles were patterned and embedded in the PMMA thin films. The presence of energetic BPO allowed for the effective thermal lithography of Ag NPs. Dark-field optical microscopy (DFOM) was utilized to directly observe the surface plasmon resonance (SPR) scattering of the SThL-patterned Ag NPs. The size of the Ag NPs and their patterning distribution were examined by transmission electron microscopy (TEM). Localized thermal analysis (LTA) identified the BPO decomposition and other thermal signatures under the in situ heating of the thermal probe. Energetic-assisted SThL in both contour-scanning and dot-matrix stamping confirms the plasmonic nanoparticle patterning in the polymer thin films, which are of great interest for plasmonic waveguides,[17,18] optical antennas,[19,20] and other SPR-related applications.[21] Most importantly, this work established a novel SThL technique with an additional joule supply that significantly improves the thermal lithography efficiency for patterning Ag NPs or other lithography materials.

EXPERIMENTAL SECTION

As summarized in Table 1, SThL samples were spin-coated from solutions of poly(methyl methacrylate) (PMMA) (M_w = 120 000, Aldrich) in methyl ethyl ketone (MEK). Energetic benzoyl peroxide (BPO) (≥97%, Fluka) was added at BPO/MMA molar ratios in the range of 0 to 0.2. Silver nitrate ($AgNO_3$) (≥99.8%, Aldrich) was separately dissolved in a small amount of ethanol before adding it to PMMA/BPO solutions. The molar ratios of BPO/$AgNO_3$ for these five samples were 0, 0.5, 1, 2, and 4, respectively. Ethanol and MEK (ACS grade, Aldrich) were dried using anhydrous magnesium sulfate prior to use. The volume ratio of the ethanol/MEK cosolvent in the spin-coating solution was approximately 1:30. Polyimide film (Kapton, Du Pont Co.) was utilized as the spin-coating and SThL substrate. The thickness of the spin-coated PMMA samples was regulated at approximately 900 ± 100 nm. Upon the completion of thermal lithography, unreacted BPO and $AgNO_3$ were removed by washing the SThL samples with water/ethanol (1:1 by vol.) solutions at least three times.

Table 1. Spin-Coating Formula and PMMA Compositions of Samples Preloaded with BPO and $AgNO_3$

sample number	PMMA (wt %) in cosolvent[a]	BPO/MMA (molar ratio)	sample number	$AgNO_3$/MMA (molar ratio)	BPO/$AgNO_3$ (molar ratio)
PMMA	1.2		PMMA-Ag	0.05	
PB025	1.2	0.025	PB025-Ag	0.05	0.5
PB050	1.2	0.050	PB050-Ag	0.05	1.0
PB100	1.2	0.100	PB100-Ag	0.05	2.0
PB200	1.2	0.200	PB200-Ag	0.05	4.0

[a]Cosolvent contains ethanol and methyl ethyl ketone at the volume ratio of 1:30.

Localized thermal analysis (LTA) and scanning thermal lithography (SThL) were performed using a Wollaston wire thermal probe[22] (Veeco, with spring constant of about 5 N/m), equipped and controlled by a NanoTA Thermal Analyzer (Anasys Instruments) and an SPM platform (Nano-R2, Pacific Nanotechnology). Polycaprolactone (T_m = 55 °C), polyethylene (T_m = 110 °C), and poly(ethylene terephthalate) (T_m = 260 °C) were utilized as melting point standards for the temperature calibration of the thermal probe. Thermal expansion profiles of three polymer standards were also individually monitored to ensure the consistent mechanical response of these thermal probe cantilevers.

RESULTS AND DISCUSSION

The thermal response of PMMA/$AgNO_3$/BPO thin films was first examined by a localized thermal analysis (LTA), otherwise known as a microthermal analysis (μTA).[23] A typical LTA measurement extracts two thermal characteristics from the surface of the sample. The first is the z-height signal (zH), which records the vertical position of the probe commonly used in the SPM system. In the case of the LTA measurement, the z-height signal sketches the thermal expansion of the material and its softening deformation as a function of temperature. The second thermal characteristic is the delta power (ΔPw) from the power consumption of the thermal probe. After the baseline calibration and reference probe subtraction, ΔPw represents the net joule energy transferred from the thermal probe to the surface of the sample. In comparison with the heat capacity measurement performed using conventional differential scanning calorimetry (DSC), the ΔPw in LTA is mainly a function of the sample thermal conductivity (k), the contact thermal conductance (D), and the probe contact area.[11,24]

As shown in Figure 1, a spin-coated pure PMMA sample with a film thickness of approximately 800 nm was examined by the LTA from room temperature to 190 °C. The measurement was initiated by maintaining the thermal probe on the surface of the sample with a SPM-controlled contact force of approximately 9.2 μN, estimated using the probe spring constant and the feedback set point. The precalibrated thermal probe was then heated at a rate of 20 °C/s, which raised the surface temperature of the sample and caused the thermal expansion, as observed in its zH profile (Figure 1). Most polymeric materials have thermal conductivities (k) and thermal diffusivities (D) on the order of 0.1−0.4 W/mK and 0.1−0.2 mm^2/s,[25] respectively, meaning that the effective heat

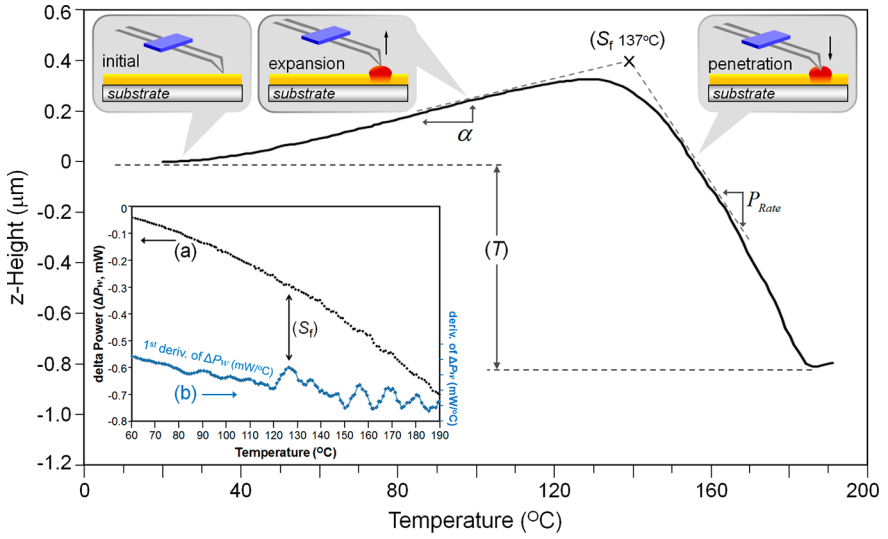

Figure 1. The *zH* profile of a PMMA thin film obtained using an LTA measurement reveals the softening temperature (S_f) and the film thickness (T). The inset illustrates (a) the corresponding ΔPw profile and (b) the first derivative of ΔPw.

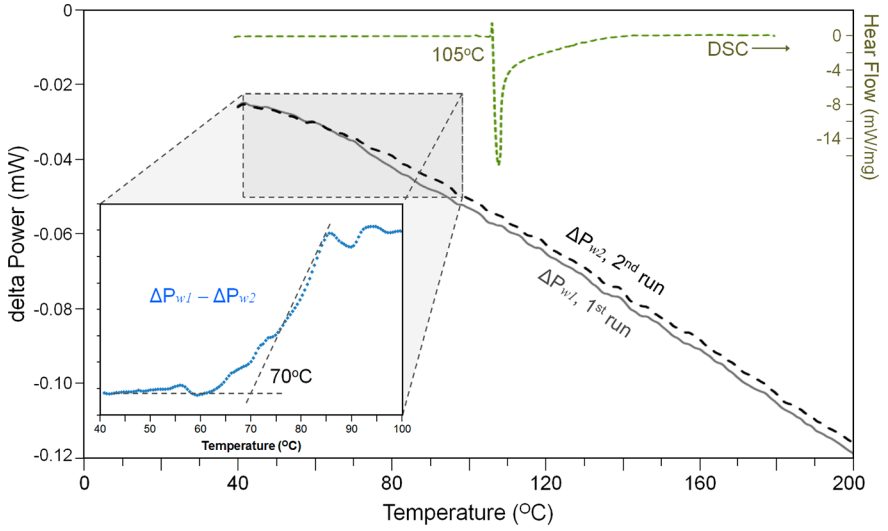

Figure 2. $\Delta Pw1$ and $\Delta Pw2$ are two sequential LTA measurements obtained at the same position of a BPO-coated Kapton surface. The profile of ($\Delta Pw1-\Delta Pw2$) in the inset reveals the initiation of the BPO decomposition at 70 °C, which is much lower than the 105 °C decomposition temperature obtained by DSC.

penetration depth is much larger than the one-micrometer thickness of the PMMA film ($k \cong 0.2$ W/mK and $D \cong 0.12$ mm^2/s).[25] Therefore, the vertical temperature gradient from the thermal probe contact point through the thin PMMA layer is negligible. The localized heating through the polymer thin film was thus considered to be steady and uniform. In addition, the slope of the *zH* profile in Figure 1 reveals the thermal expansion coefficient (α) of the PMMA thin film sample coated on a Kapton substrate. In Figure 1, α was found to be 4.4×10^{-6} (K^{-1}), approximately 1 order of magnitude lower than the thermal expansion coefficient of the bulk PMMA sample.

The continuous heating of the thermal probe results in polymer softening at a higher temperature. For a glassy polymer, such as PMMA, the material softening is associated with its glass transition temperature. Above this temperature, the probe contact force suppresses the PMMA thermal expansion and triggers a decrease in *zH* with a detectable onset softening at approximately 137 °C (marked with S_f in Figure 1). For a thin film sample, the decrease in *zH* was eventually interrupted by the substrate when the probe penetrated the entire polymer layer. Furthermore, the maximum decrease in *zH* from the initial probe position to its contact with the substrate (marked with T) is in agreement with the original film thickness determined by the SPM morphology scan to the partially peel-off sample.

At the softening temperature, the slightly submerged probe increased the probe contact area, which simultaneously promoted the tip-to-sample heat transfer with a traceable thermal signature in ΔPw. The inset of Figure 1 illustrates the ΔPw profile of the PMMA sample as a function of probe temperature. Variations in the heat transfer to a polymer thin film were less observable in the raw ΔPw signal (profile a). However, the first derivative of ΔPw (see profile b) depicts a hidden fluctuation in the heat flow and a transition temperature at 126 °C. This temperature was approximately 10° lower than the *zH* softening temperature (137 °C), indicating that the thermal response of the material was instinctively faster than its dimensional expansion or softening, especially when the

dx.doi.org/10.1021/am302287q | ACS Appl. Mater. Interfaces 2013, 5, 120−127

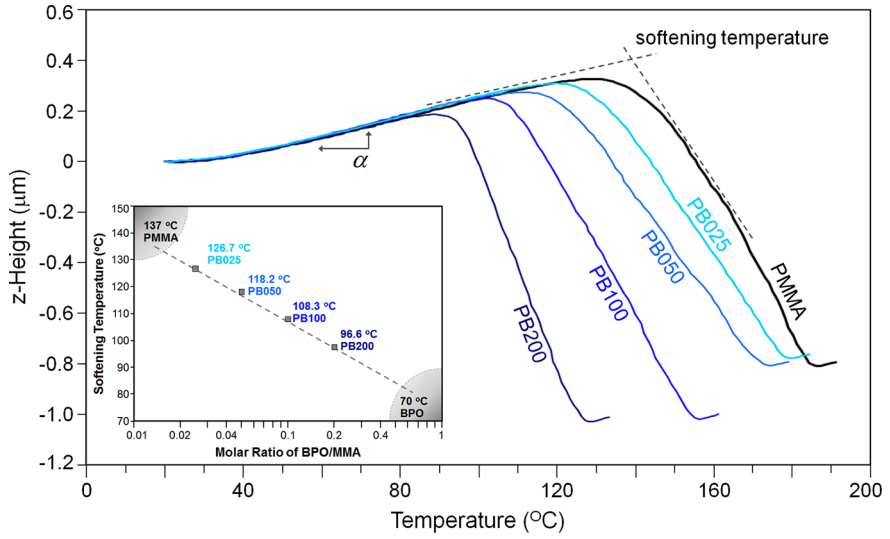

Figure 3. *zH* profiles of PMMA and four PMMA/BPO samples with identical thermal expansion coefficients (α) prior to their softening. In the inset, the softening temperatures are linearly proportional with the BPO/MMA molar ratios on a logarithmic scale.

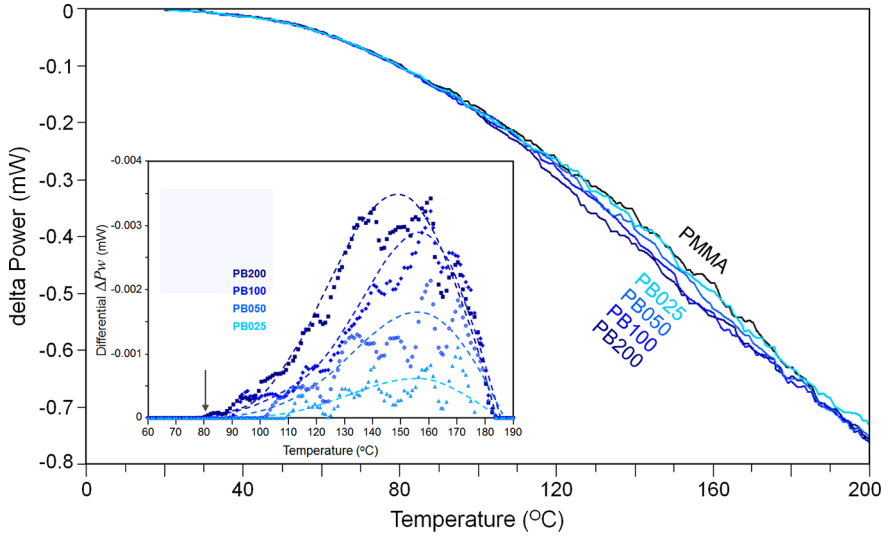

Figure 4. ΔPw profiles of PMMA and four PMMA/BPO samples. The inset shows the differential ΔPw of four PMMA/BPO samples individually subtracted from the ΔPw of the PMMA sample.

measurement was carried out under a relatively fast heating rate.

In a separate experiment, a dilute BPO/ethanol solution was spin-coated on a Kapton substrate. The resulting thin BPO coating was treated with two sequential LTA measurements at the same position (see Figure 2). Presumably, the first LTA measurement up to 200 °C ($\Delta Pw1$) thermally scavenged all energetic BPO near the testing position. In the second run of the LTA ($\Delta Pw2$), no BPO reagent was detected at this position. Accordingly, the ΔPw difference between the first and second LTA measurements ($\Delta Pw1-\Delta Pw2$) revealed the temperature-dependent joule release of the thin BPO coating. In the inset of Figure 2, the ($\Delta Pw1-\Delta Pw2$) curve identifies the BPO "take-off" temperature as approximately 70 °C in the presence of direct thermal probe contact and a heating ramp of 20 °C/s. This temperature was lower than the 80 °C decomposition temperature determined by free radical formation[26] and much lower than the 105 °C obtained using the conventional DSC measurement (10 °C/min heating ramp, also in Figure 2).

LTA investigations in the presence of energetics were conducted on PMMA/BPO thin film samples prepared with the BPO/MMA molar ratios of 0.025, 0.05, 0.1, and 0.2 (see formula details in Table 1). The thickness of the four spin-coated PMMA/BPO samples on Kapton substrates was maintained at 900 ± 100 nm, similar to that of the pristine PMMA sample. As shown in Figure 3, the *zH* profiles of pure PMMA and four PMMA/BPO samples exhibited identical thermal expansion profiles with a consistent thermal expansion coefficient of 4.4×10^{-6} K^{-1}. This observation indicated that the energetic BPO molecules within PMMA essentially remained inert prior to their thermal decomposition. At or above 80 °C, the exothermal joule energy from the energetic BPO exhibited a significant influence on the *zH* profiles. An increase in the BPO loadings was accompanied by a remarkable decline in the *zH* softening temperatures from the original 137 °C of the PMMA film to a minimum temperature of 96.6 °C

dx.doi.org/10.1021/am302287q | ACS Appl. Mater. Interfaces 2013, 5, 120−127

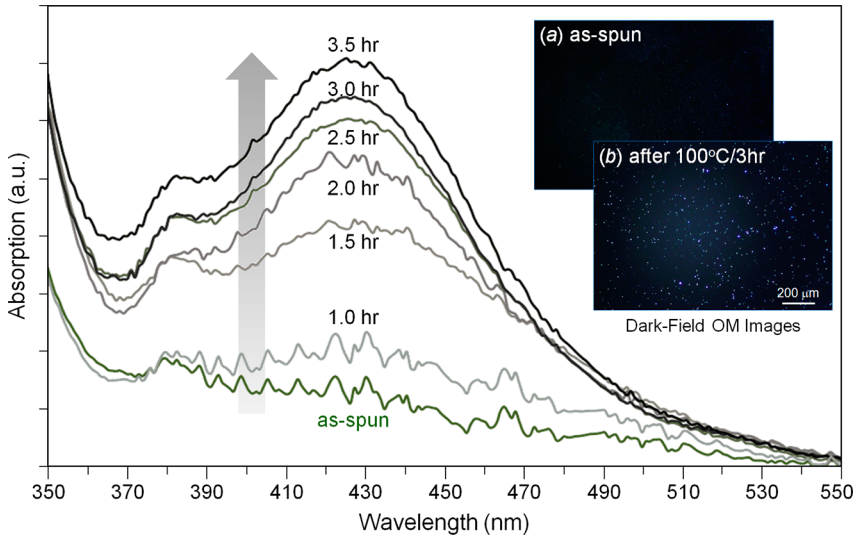

Figure 5. SPR absorption spectra of PB200-Ag samples as a function of isothermal periods at 100 °C. Two DFOM images on the right show (a) the as-spun PB200-Ag and (b) the heated PB200-Ag (at 100 °C for 3 h).

for sample PB200. In the inset of Figure 3, the softening temperatures of four PMMA/BPO samples changed linearly with respect to their BPO/MMA molar ratios on a logarithmic scale. This linear profile can be extended leftward to the 137 °C softening temperature of the pure PMMA thin film, and rightward to the 70 °C thermal decomposition of the pure BPO layer.

Note that the *zH*-recorded softening in an LTA measurement was based on the precalibrated probe temperature. In the presence of additional joule heating, the actual localized temperature in the PMMA/BPO samples was presumably higher than the temperature recorded by the probe. In other words, the softening of PMMA/BPO samples still required the specific temperature of 137 °C. In addition, the BPO extra energy stimulated the measurement with the temperature increase by as much as 40 °C (between 96.6 and 137 °C) higher than the probe temperature. This exothermal stimulation could also be observed in the Δ*Pw* signal. Similar to the two sequential LTA measurements of the BPO coating sample (Figure 2), the differential Δ*Pw* profiles of the four PMMA/BPO samples shown in Figure 4 were obtained individually by subtracting from the pure PMMA Δ*Pw*. These differential Δ*Pw* profiles and their curve fittings (see the inset) revealed the initiation of BPO decomposition. The 80 °C "take-off" temperature for the PB200 sample and the slightly higher temperatures for the other three samples agreed with the previous *zH*-recorded softening. Curve fittings in the inset also showed the highest differential Δ*Pw* for sample PB200, suggesting that this sample exhibited the highest exothermal energy detected by the thermal probe. With a lower loading of the energetic compound, sample PB025 had the lowest differential Δ*Pw* value. Note that the sample softening in the LTA is always accompanied by the submerging of the probe and an increase in the contact area. Therefore, the differential Δ*Pw* curve fittings in the inset can only be used for qualitative analysis and are not quantitative measurements of the exothermic energy gains.

In addition to the softening temperature reduction, the addition of energetics in SThL fabrication also enhanced the thermally induced chemical reaction. In this study, the SThL fabrication incorporated the synthesis of silver nanoparticles from the thermal decomposition of the silver nitrate precursor preloaded in the PMMA thin film. $AgNO_3$ concentrations were fixed at the molar ratio of 5% with respect to the MMA repeat unit. The addition of energetic BPO was controlled at the same concentrations as in the previous PB025, PB050, PB100, and PB200 samples. BPO/$AgNO_3$ molar ratios for the four PMMA/BPO/$AgNO_3$ samples were 0.5, 1, 2, and 4, respectively (details in Table 1). The thickness of the spin-coated samples was also maintained (regulated) at 900 ± 100 nm. The thermal decomposition of $AgNO_3$ moieties in the solidified PMMA coatings was first conducted by a bulk heating in a 100 °C oven. The formation of Ag NPs was sequentially monitored by their localized surface plasmon resonance (SPR) shown in the UV−vis absorption spectra. For example, Figure 5 demonstrates that PB200-Ag samples exhibited a steady SPR band growth at 425 nm, indicating an increase in the population of Ag NPs as a function of the isothermal periods. The DFOM image of the heated PB200-Ag sample (3 h at 100 °C) (the inset image b) highlights the illuminant spots scattered by the presence of Ag NPs, contrary to the as-spun PB200-Ag with no trace of scattering spots (the inset image a).

Time-dependent SPR spectra of the other four samples were also examined by the same 100 °C isothermal treatments. All samples exhibited intensified SPR with consistent SPR bands centered at 425 ± 3 nm. Figure 6 illustrates the SPR growth for five samples as a function of the isothermal duration. In the first hour of 100 °C heating, the SPR of Ag NPs was barely observed for all samples. After that, the gradually increasing SPR signal confirmed the formation of Ag NPs. Samples with zero and low BPO loading (PMMA-Ag and PB025-Ag) had moderated SPR growth over the course of the 3.5 h heating process. Nevertheless, the other three samples with higher BPO concentrations (PB050-Ag, PB100-Ag, and PB200-Ag) exhibited a rapidly elevated SPR, started after 1.5 h of heating. In Figure 6, the final SPR intensities after 3.5 h heating were then projected to the screen on the right, shadowing the energetic-assisted reactions altered by the presence of BPO. The discrete gap in profile a (Figure 6) revealed a critical BPO concentration of approximately 0.05 wt %. Below this concentration, sample PB025-Ag exhibited deficient joule energy that was then quickly dissipated. Accordingly, the bulk heating process in this sample

dx.doi.org/10.1021/am302287q | *ACS Appl. Mater. Interfaces* 2013, 5, 120−127

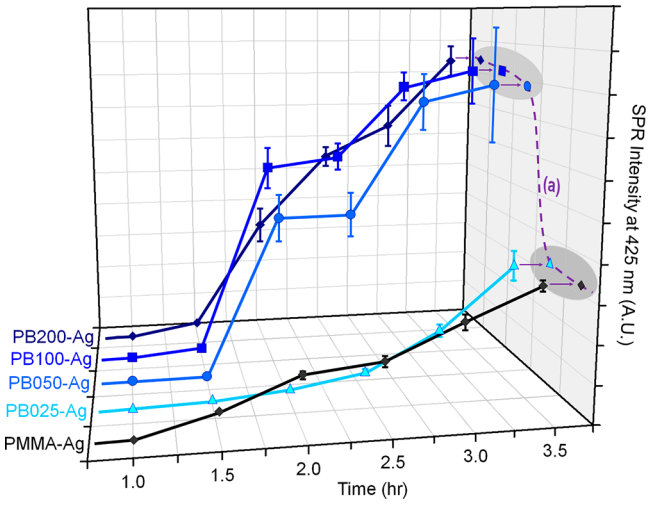

Figure 6. SPR absorption intensity growth for the five samples as a function of 100 °C isothermal periods. PMMA-Ag and PB025-Ag with BPO concentrations of less than 0.05 wt % exhibited moderate SPR growth profiles. The other three samples with higher BPO loadings exhibited rapid SPR increases. The critical BPO concentration is illustrated on curve a projected on the right.

was not improved, and its SPR growth profile was similar to the one for PMMA-Ag containing no energetic BPO. For the other three samples with a higher BPO content, a noticeable SPR increase indicates that the BPO joule release occurred on a larger scale than the cooling did. The net joule gain drove the effective temperature higher than 100 °C, causing an acceleration of $AgNO_3$ decomposition.

In contrast with the isothermal bulk synthesis of Ag NPs in the oven, SThL involves a mobile heating probe with a tip diameter as low as 2 μm, in which the small contact area substantially diminishes the effective joule exchange. Therefore, successful SThL demands a higher probe temperature and/or a slower scanning rate. With the addition of energetics, the extra energy further compensates the joule shortage and improves the localized heating mechanism.

Five spin-coated samples (PMMA-Ag, PB025-Ag, PB050-Ag, PB100-Ag, and PB200-Ag) were utilized in SThL. An SThL process was typically performed at a given probe temperature and a controlled probe scanning rate. Here, the thermal probe was isothermally controlled at 100, 150, 200, 250, and 300 °C. For each SThL trial, three parallel lines were sequentially lithographed with variations in probe scanning rates maintained at 0.1, 0.2, and 0.4 μm/s. After the thermal lithography process, samples were washed with water/ethanol solutions (1:1 by vol.) three times to ensure the complete removal of unreacted $AgNO_3$ and BPO. The resulting PMMA thin films with SThL-patterned Ag NPs were first examined by the DFOM (see Figure 7). Scattering spots shown in the DFOM images represent the distributions of Ag NPs in the three horizontal lines. Although the DFOM does not offer a precise quantitative analysis of the Ag NP populations, the images shown in Figure 7 still reflected the SThL performances and the Ag NP populations. In the previous isothermal bulk synthesis, the energetic-assisted Ag NP formation required at least 0.05 wt % BPO loading. The same samples in the SThL fabrication process necessitated higher probe temperatures or higher BPO content. SThL samples with BPO loading below 0.05 wt % and probe temperature below 150 °C exhibited no detectable Ag NPs in their DFOM (see the Supporting Information for six more DFOM images). SThL successfully synthesized the Ag NPs for samples containing more than 0.1 wt % BPO or at a probe temperature higher than 200 °C. As for the three SThL horizontal lines, the probe scanning rates showed no obvious influence on the Ag NP populations shown in each DFOM image. Presumably, the isothermal scanning probe had a steady joule exchange rate. For a given lithography length, a slow

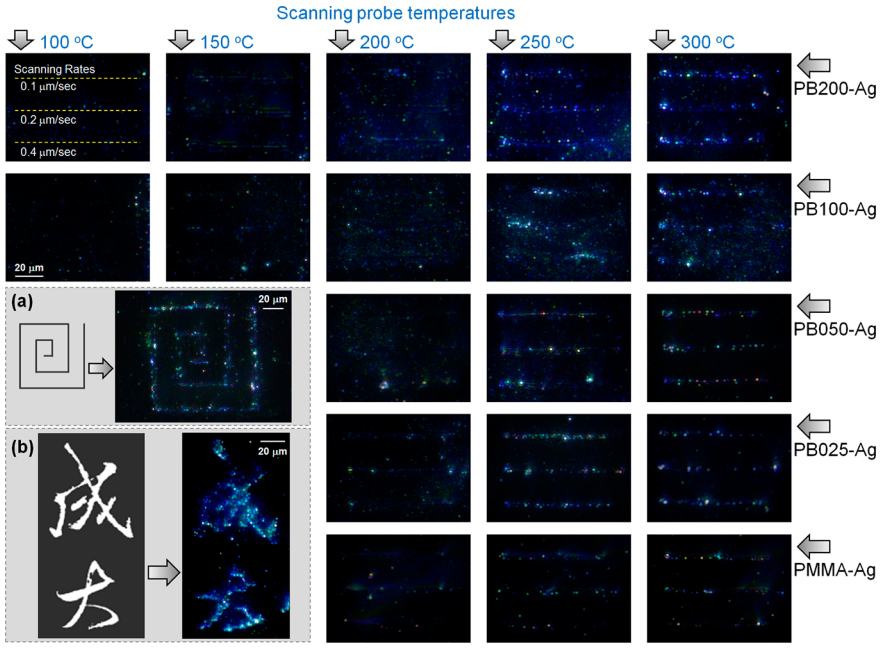

Figure 7. DFOM images illustrate the SPR scattering of patterned silver nanoparticles in the PMMA-Ag and four other PMMA/BPO/$AgNO_3$ samples. Three horizontal lines in each image represent the SThL process at a given probe temperature and scanning rate. Two additional DFOM images reveal (a) square spiral SThL with a contour scattering distance of up to 500 μm and (b) a dot-matrix stamping of two Chinese characters (National Cheng Kung University abbreviation).

dx.doi.org/10.1021/am302287q | ACS Appl. Mater. Interfaces 2013, 5, 120−127

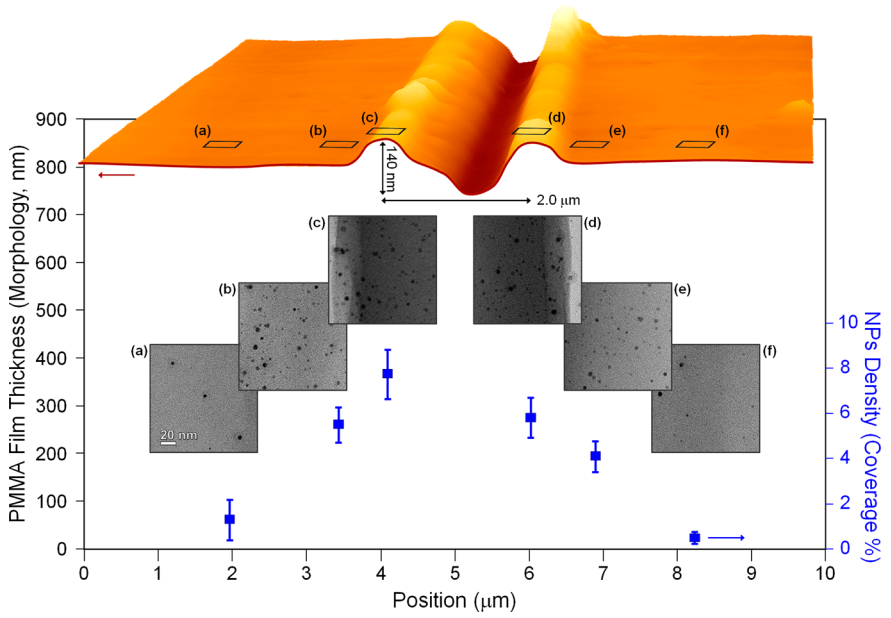

Figure 8. Surface morphology (top) of sample PB200-Ag demonstrating SThL at 250 °C produced a peak-to-valley dimension of 140 nm and a peak-to-peak dimension of 2 μm. TEM images were obtained at the six positions labeled a–f. Nanoparticle coverage (%) from the TEM images illustrates the distribution of silver nanoparticles.

probe scanning process converged more energy on the sample, and vice versa. However, the time-dependent cooling also followed the same trend. As a result, the SThL heating and the counter cooling maintained their balance at the probe scanning rates in the range of 0.1 and 0.4 μm/s.

Two more DFOM images shown in images a and b in Figure 7 depict the Ag NP patterns from sample PB050-Ag. The first image (a) is a square spiral pattern lithographed using a 250 °C probe at a 0.4 μm/sec scanning rate. The continuous contour scanning distance in this experiment was more than 500 μm. The second image (b) depicts two Chinese characters (National Cheng Kung University abbreviation) constructed by a program-controlled serial stamping that composed the desired dot-matrix pattern. The thermal probe was isothermally maintained at 250 °C, and each thermal stamping was held for 0.5 s. Both DFOM images demonstrate successful energetic-assisted SThL, which is capable of creating any desired pattern or geometry.

Figure 8 shows the surface morphology of sample PB050-Ag after typical 250 °C SThL with a scanning rate of 0.4 μm/s. Compared with its original 800 nm film thickness, the SThL process scratched the PMMA surface with a maximum peak-to-valley variation of 140 nm and an average line width of 2.0 μm (peak-to-peak), which is proportional to the scale of the 2 μm tip of the microthermal probe. This SThL sample was carefully relocated to the gold grid mesh for the TEM and EDS examinations. EDS spectra (data not shown) identified the presence of silver after the SThL and washing processes. TEM images taken at the six positions labeled a–f in Figure 8, revealed the Ag NPs and their populations. Approximately three micrometers away from the SThL center line (positions a and f), the Ag NPs exhibited a low NP density of less than 1% coverage in accordance with the Ag NP projected area in the TEM images. Near the SThL center line, the Ag NP populations reached a maximum of 8% coverage. Because the original formula contained only 5% $AgNO_3$ in the solidified PMMA, the 8% coverage of Ag NPs suggests that the $AgNO_3$ decomposition reached an optimized conversion at the position close to the SThL center line. Despite the distribution of nanoparticles near the SThL center line, no size variations of Ag NPs were found in the six locations. In addition, the diameters of SThL-synthesized Ag NPs were measured to be in the narrow range of 5 ± 1.0 nm. It was believed that the low $AgNO_3$ concentration and relatively low SThL temperature had constrained the silver ion diffusion and individual nanoparticle growth in the solid state. A further increase in the precursor loading will improve the nanoparticle density.

CONCLUSIONS

Energetic-assisted scanning thermal lithography was successfully demonstrated in poly(methyl methacrylate) thin films preloaded with benzoyl peroxide and silver nitrate. Exothermal joule energy from peroxide decomposition resulted in the in situ released of energy to compensate the joule shortage and the rapid cooling in the lithography thin films. The peroxide decomposition at approximately 80 °C was identified by a localized thermal analysis. Polymer softening temperatures were found to decrease with increasing concentration of energetic peroxides, suggesting that the extra joule energy had stimulated the localized temperature by as much as 40 °C for the samples containing a 0.2% molar concentration of peroxide. The addition of silver nitrate in the lithography samples facilitated thermally induced decomposition to form silver nanoparticles. Dark-field optical microscopy revealed the surface plasmon resonance scattering of patterned silver nanoparticles in both contour-scanning and dot-matrix stamping fabrication. The lithographic resolution in this work was approximately 2 μm, proportional to the tip size of the thermal probe. Furthermore, the diameter of the silver nanoparticles was in the narrow range of 5 ± 1.0 nm. A study of lithography temperatures and peroxide concentrations indicated that the addition of energetics successfully improved the efficiency of the scanning thermal lithography technique.

dx.doi.org/10.1021/am302287q | ACS Appl. Mater. Interfaces 2013, 5, 120–127

■ ASSOCIATED CONTENT

Supporting Information

DFOM images of SThL samples with BPO loading below 0.05 wt % and probe temperature below 150 °C. This material is available free of charge via the Internet at http://pubs.acs.org.

■ AUTHOR INFORMATION

Corresponding Author

*E-mail: changshu@mail.ncku.edu.tw.

Notes

The authors declare no competing financial interest.

■ ACKNOWLEDGMENTS

The authors are grateful for the financial supports from the National Science Council (NSC 100-2120-M-006-006 and NSC 100-2221-E-006-150) and the NCKU Project of Promoting Academic Excellence & Developing World Class Research Centers (D101-23010).

■ REFERENCES

(1) Bottomley, L. A. *Anal. Chem.* **1998**, *70*, 425R−475R.
(2) Szoszkiewicz, R.; Okada, T.; Jones, S. C.; Li, T.-D.; King, W. P.; Marder, S. R.; Riedo, E. *Nano Lett.* **2007**, *7*, 1064−1069.
(3) Ogino, T.; Nishimura, S.; Shirakashi, J. *Jpn. J. Appl. Phys.* **2008**, *47*, 712−714.
(4) Oliveira, A. B.; Medeiros-Ribeiro, G.; Azevedo, A. *Nanotechnology* **2009**, *20*, 345301.
(5) Credgington, D.; Fenwick, O.; Charas, A.; Morgado, J.; Suhling, K.; Cacialli, F. *Adv. Funct. Mater.* **2010**, *20*, 2842−2847.
(6) Demers, L. M.; Ginger, D. S.; Park, S. J.; Li, Z.; Chung, S. W.; Mirkin, C. A. *Science* **2002**, *296*, 1836−1838.
(7) Wang, H.-T.; Nafday, O. A.; Haaheim, J. R.; Tevaarwerk, E.; Amro, N. A.; Sanedrin, R. G.; Chang, C.-Y.; Ren, F.; Pearton, S. J. *Appl. Phys. Lett.* **2008**, *93*, 143105.
(8) Uehara, H.; Asakawa, T.; Kakiage, M.; Yamanobe, T.; Komoto, T. *Langmuir* **2006**, *22*, 4985−4991.
(9) Hua, Y.; Saxena, S.; Henderson, C. L.; King, W. P. *J. Micro/Nanolithogr., MEMS, MOEMS* **2007**, *6*, 023012.
(10) Fenwick, O.; Bozec, L.; Credgington, D.; Hammiche, A.; Lazzerini, G. M.; Silberberg, Y. R.; Cacialli, F. *Nat. Nanotechnol.* **2009**, *4*, 664−668.
(11) Majumdar, A. *Annu. Rev. Mater. Sci.* **1999**, *29*, 505−585.
(12) Duvigneau, J.; Schoenherr, H.; Vancso, G. J. *ACS Nano* **2010**, *4*, 6932−6940.
(13) Kim, K.; Jeong, W.; Lee, W.; Reddy, P. *ACS Nano* **2012**, *6*, 4248−4257.
(14) Tolk, M.; Fenwick, O.; Ahmad, S.; Cacialli, F. *J. Appl. Phys.* **2012**, *111*, 124317.
(15) Mossino, R. *Ceram. Int.* **2004**, *30*, 311−332.
(16) Aruna, S. T.; Mukasyan, A. S. *Curr. Opin. Solid State Mater. Sci.* **2008**, *12*, 44−50.
(17) Maier, S. A.; Kik, P. G.; Atwater, H. A.; Meltzer, S.; Harel, E.; Koel, B. E.; Requicha, A. A. G. *Nat. Mater.* **2003**, *2*, 229−232.
(18) Fevrier, M.; Gogol, P.; Aassime, A.; Megy, R.; Delacour, C.; Chelnokov, A.; Apuzzo, A.; Blaize, S.; Lourtioz, J.-M.; Dagens, B. *Nano Lett.* **2012**, *12*, 1032−1037.
(19) Muhlschlegel, P.; Eisler, H.-J.; Martin, O. J. F.; Hecht, B.; Pohl, D. W. *Science* **2005**, *308*, 1607−1609.
(20) Ross, B. M.; Wu, L. Y.; Lee, L. P. *Nano Lett.* **2011**, *11*, 2590−2595.
(21) Hicks, E. M.; Lyandres, O.; Hall, W. P.; Zou, S.; Glucksberg, M. R.; van Duyne, R. P. *J. Phys. Chem. C* **2007**, *111*, 4116−4124.
(22) Harding, L.; Wood, J.; Reading, M.; Craig, D. Q. M. *Anal. Chem.* **2007**, *79*, 129−139.
(23) Tsukruk, V. V.; Gorbunov, V. V.; Fuchigami, N. *Thermochim. Acta* **2003**, *395*, 151−158.
(24) Kuo, C.; Chen, C.-C.; Bannister, W. *Thermochim. Acta* **2003**, *403*, 115−127.
(25) Lyon, R. E. In *Handbook of Building Materials for Fire Protection*; Harper, C., Ed.; McGraw-Hill: New York, 2004; Chapter 3, 3.1−3.51.
(26) Wang, W.; Wang, L.; Chen, X.; Yang, Q.; Sun, T.; Zhou, J. *Macromol. Mater. Eng.* **2006**, *291*, 173−180.